PNAS RESEARCH ARTICLE | BIOPHYSICS AND COMPUTATIONAL BIOLOGY

Virion-associated influenza hemagglutinin clusters upon sialic acid binding visualized by cryoelectron tomography

Qiuyu J. Huang[a], Ryan Kim[a], Kangkang Song[a], Nikolaus Grigorieff[b], James B. Munro[a,c], Celia A. Schiffer[a,1], and Mohan Somasundaran[a,1]

Contributed by Celia A. Schiffer; received December 17, 2024; accepted March 12, 2025; reviewed by Tijana Ivanovic and Dmitry Lyumkis

Influenza viruses are enveloped, negative-sense single-stranded RNA viruses covered in a dense layer of glycoproteins. Hemagglutinin (HA) accounts for 80 to 90% of influenza glycoprotein and plays a role in host cell binding and membrane fusion. While previous studies have characterized structures of purified receptor-free and receptor-bound HA, the effect of receptor binding on HA organization and structure on virions remains unknown. Here, we used cryoelectron tomography to visualize influenza virions bound to a sialic acid receptor mimic. Overall, receptor binding did not result in significant changes in viral morphology; however, we observed rearrangements of HA trimer organization and orientation. Compared to the even interglycoprotein spacing of unliganded HA trimers, receptor binding promotes HA trimer clustering and the formation of a triplet of trimers. Subtomogram averaging and refinement yielded 8 to 10 Å reconstructions that allowed us to visualize specific contacts between HAs from neighboring trimers and identify molecular features that mediate clustering. Taken together, we present structural evidence that receptor binding triggers clustering of HA trimers, revealing an additional layer of HA dynamics and plasticity.

cryoelectron tomography | hemagglutinin | influenza

Significance

Influenza hemagglutinin (HA) is responsible for two crucial steps in the viral life cycle—receptor binding on the host cell and membrane fusion. Coordination of several HAs is required to carry out efficient cellular uptake and fusion. We use cryoelectron tomography, neural networks, and subtomogram averaging to directly visualize the coordination of HA induced by receptor binding. When receptor is bound three adjacent HAs cluster together through specific head domain interactions. This visualization provides insights into the molecular mechanism by which influenza uses HA avidity to enter the cell during viral infection.

Influenza viruses are highly contagious respiratory pathogens that cause approximately 1 billion cases of flu in humans each year. Influenza initiates infection through receptor-mediated endocytosis, where the trimeric hemagglutinin (HA) glycoprotein binds sialic acid-containing host cellular receptors (1). Individual interactions between HA and sialic acid are weak; polyvalent interactions between multiple simultaneous HA–sialic acid binding events are required for successful viral entry (2).

HA is a 200-kDa protein that is structurally divided into the globular domain (HA1), which includes the sialic acid receptor binding site, and the HA2 domain, which contains the fusion peptide, a hydrophobic stretch of amino acids that inserts into the endosomal membrane during fusion with the viral envelope (3). Structural studies of the soluble HA ectodomain revealed that sialic acid binding does not induce large structural rearrangements in HA ectodomains (4–6). In contrast, biophysical analyses of full-length HA on the virion surface indicated that sialic acid binding induces movement of the fusion peptide (7). This observation emphasizes that ectodomain structures provide only a limited amount of insight into the dynamic processes of HA–receptor interaction, and a full understanding of the HA-mediated virus binding and entry into cell requires structural analysis of HA on intact virions. Previous cryoelectron tomography (cryoET) studies, including our work, have shown that spherical influenza virions carry 300 to 500 glycoproteins, with consistent interglycoprotein spacing of between 9 and 11 nm (8–10). Moreover, biophysical studies showed that hemifusion with the target membrane requires cooperativity among three to four neighboring HA trimers (11–14), suggesting that HA trimers form intertrimer interactions to facilitate the process. In this context, receptor binding may promote HA cooperativity and clustering. However, the effects of receptor binding on HA structure in the context of virions have not previously been investigated.

In the current study, we employed cryoET for ultrastructural studies of the A/Puerto Rico/8/34 (H1N1) influenza A virus (henceforth referred to as PR8) incubated with a sialic acid-containing receptor mimic. While receptor binding did not result in significant changes in viral morphology, we observed formation of HA clusters composed of triplet of trimers in a receptor-binding dependent manner. Within this assembly, HAs form direct interactions with HA protomers of neighboring trimers, using both polar and electrostatic interactions. Our study reveals that HA receptor binding can induce cluster formation, suggesting that disrupting this clustering may offer a strategy for targeting influenza virus.

Author affiliations: [a]Department of Biochemistry and Molecular Biotechnology, University of Massachusetts Chan Medical School, Worcester, MA 01605; [b]RNA Therapeutics Institute, University of Massachusetts Chan Medical School, Worcester, MA 01605; and [c]Department of Microbiology, University of Massachusetts Chan Medical School, Worcester, MA 01605

Preprint server: This manuscript has been deposited to bioRxiv and can be accessed at the following DOI: http://doi.org/10.1101/2024.10.15.618557.

Author contributions: Q.J.H., N.G., J.B.M., C.A.S., and M.S. designed research; Q.J.H., R.K., and K.S. performed research; Q.J.H. and J.B.M. contributed new reagents/analytic tools; Q.J.H. analyzed data; and Q.J.H., C.A.S., and M.S. wrote the paper.

Reviewers: T.I., National Institute of Allergy and Infectious Diseases Division of Intramural Research; and D.L., Salk Institute for Biological Studies.

The authors declare no competing interest.

[1]To whom correspondence may be addressed. Email: celia.schiffer@umassmed.edu or mohan.somasundaran@umassmed.edu.

This article contains supporting information online at https://www.pnas.org/lookup/suppl/doi:10.1073/pnas.2426427122/-/DCSupplemental.

Published April 17, 2025.

Results

CryoET of Receptor-Bound Influenza Virus Reveals Little Changes in Viral Morphology. To evaluate whether receptor binding causes structural rearrangements in HA or changes in viral morphology, we obtained tilt-series of PR8 with and without the receptor mimic sialylneolacto-N-tetraose c (LSTc). LSTc is a glycan containing a terminal α2–6-linked sialic acid; it productively binds and inhibits PR8 and other influenza A virus strains (15). Prior to plunge freezing, influenza virions were incubated with 100 μM or 6.5 mM of LSTc for at least 15 min to reach equilibration (*SI Appendix,* Table S1).

Tomogram reconstruction of PR8 and PR8-LSTc allowed for clear identification of virus components (Fig. 1 and Movies S1 and S2). Similar to previous cryoET studies at neutral pH (8, 16, 17), PR8 virions are membranous viruses of spherical or oval morphology. Beneath the lipid bilayer, most virions showed clear density for the matrix protein (M1) protein layer, as well as the viral ribonucleoprotein (vRNP) complex. We were also able to discern the two distinct glycoproteins, HA and NA, based on the clear difference in their size and shape with HA appearing taller and cylindrical (Fig. 1 *A* and *B*). To quantify potential morphological differences between receptor-free and receptor-bound virions, we applied the convolutional neural network (CNN) analysis pipeline we previously developed (*SI Appendix,* Fig. S1) (8). Consistent with our recent findings, influenza virions were extremely pleomorphic (Fig. 1 *C* and *D*). The median long- and short-axis measurements were 124 nm and 106 nm for receptor-free, and 129 nm and 108 nm for receptor-bound virions, with the median axial ratio of both populations of 1.1 (*SI Appendix,* Tables S3 and S4). Therefore, we concluded that receptor binding does not result in large morphological changes in influenza virions.

Receptor Binding Promotes Asymmetrical Clustering of Neighboring HA Trimers. To investigate dynamic changes in HA ordering and structure upon receptor binding, we conducted reference-free subtomogram averaging on receptor-free and LSTc-bound HAs. We analyzed virions where both the M1 layer and the vRNP density were present, as influenza virions missing either component would be less functionally relevant. Since influenza glycoproteins are perpendicular to the viral membrane, initial Euler angles can be estimated using the surface normal of HA coordinates picked using the CNN pipeline (*SI Appendix,* Fig. S2). These coordinates and angles were used to extract bin4 subtomograms using Warp and subjected to subtomogram refinement within Relion4 with C1 symmetry (18, 19). Several rounds of 2D classification were carried out to discard outliers and junk particles (*SI Appendix,* Figs. S3 and S4). Both HA and HA+LSTc reconstructions revealed

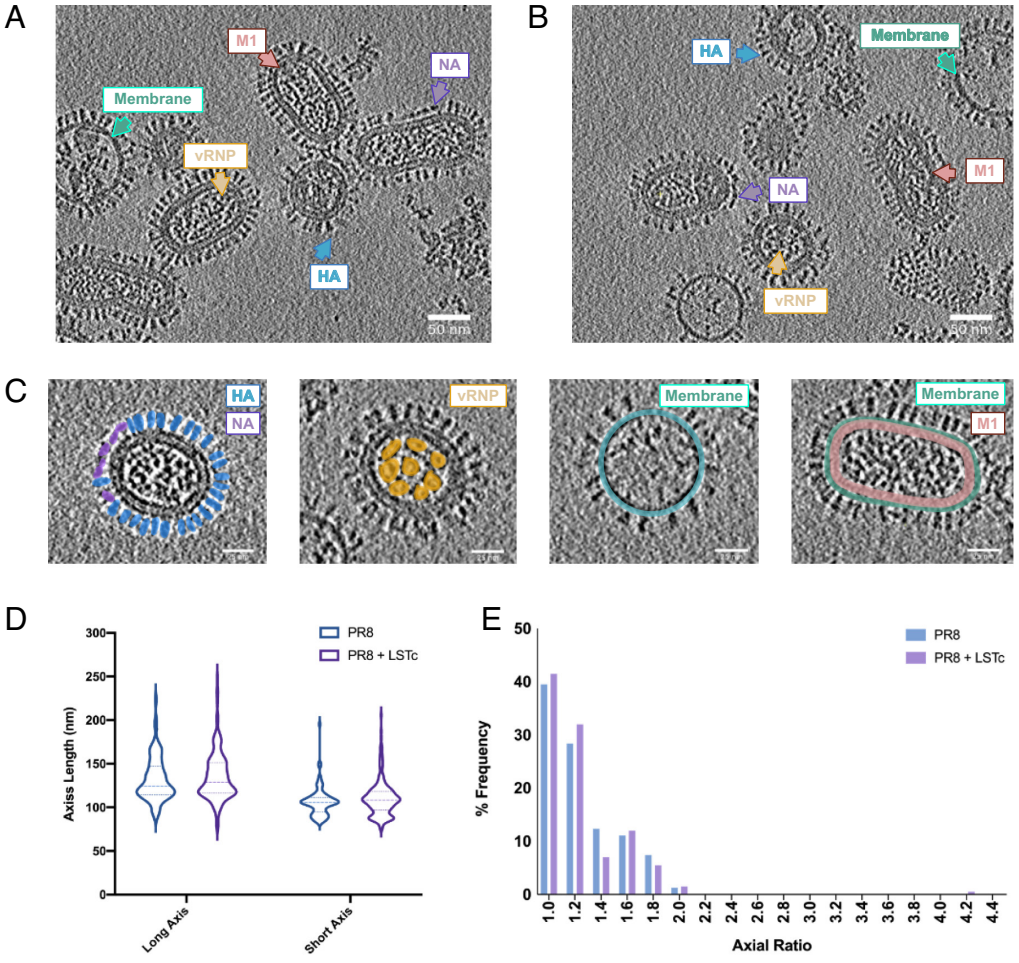

Fig. 1. Cryoelectron tomography reveals little morphological difference between influenza virions incubated with soluble receptor mimic. (*A* and *B*) Central slice through representative tomogram of (*A*) PR8 virions or of (*B*) PR8 virions with 100 μM LSTc. (Scale bars, 50 nm.) Cyan arrow points to the viral membrane, salmon arrow points to the M1 protein, yellow for the vRNP complex, and blue or purple for the HA or NA glycoproteins. (*C*) Visualization for each influenza structural component. HA is shown in blue, NA in purple, vRNP complexes in orange, viral membrane in cyan, and M1 protein in salmon. (*D*) Violin plot for long- and short-axis measurements of PR8 virions with and without LSTc. *Middle* dotted line indicates the median value; *Top* and *Bottom* dotted lines indicate interquartile range. Width of the plot correlates with the number of particles at that value. (*E*) Histogram of axial ratios of PR8 virions.

a glycoprotein array, where clear density was shown for a patch of 7 to 10 HA trimers and the viral membrane (Fig. 2). At this resolution, the distinct three-fold symmetry had only emerged for the central HA of the unliganded HA reconstruction (Fig. 2 *A* and *B*). Peripheral HAs appeared as cylindrical density and their three protomers were indistinguishable (Fig. 2 *A* and *B*). This observation contrasted with LSTc-bound HA, where distinct threefold symmetry was shown for not only the central HA but two more HAs on either side (Fig. 2 *C* and *D*). Thus, receptor binding induced rearrangement on the viral surface with neighboring HAs oriented toward each other to form a triplet of HA trimers (Fig. 2 *C* and *D*).

To characterize this arrangement of HA trimers further, we calculated the inter-HA distance between the central HA and its two closest neighbors in both receptor-free and receptor-bound structures (*SI Appendix,* Fig. S5 and Table S5). Receptor-free HA had a narrow distribution of inter-HA spacing, with the median distance between the central HA and its two closest neighbors between 84 Å and 91 Å, with an interquartile range of 80 to 87 Å and 87 to 95 Å, respectively. The distribution of inter-HA distances in receptor-bound HA was wider, with interquartile range of 68 to 80 Å and 73 to 85 Å. We also saw a general decrease in the spacing between the three central HAs, with the central HA on average 10 Å and 12 Å closer to its two neighbors. Upon 2D classification of the HA trimer array, we observed classes in which the central HA pivoted closer to either adjacent HA when compared with the consensus reconstruction (*SI Appendix,* Fig. S6). This variance is likely caused by dynamic HA rearrangements upon receptor binding, suggesting that instead of inducing structural rearrangements within individual protomers or within the HA trimer, receptor binding induces HA clustering. Moreover, this observation also shows that instead of HA moving laterally across the viral membrane, it is more likely to be tilting toward and away from its HA trimer neighbors. As a result, there may be regions where HA heads are closer together on the viral membrane due to tilting, but since HA trimers are anchored not only into the lipid membrane but also M1, overall influenza surface density should not be greatly affected.

Subtomogram Average at Subnanometer Resolution of PR8 HA Reveals Domain Organization of Virion-Anchored HA. From the low-resolution HA array, we continued refinement for the central HA trimer with C1 symmetry. Aligned subtomograms were gradually unbinned and local refinement with 2D classification steps were conducted using a focused mask in Relion (*SI Appendix,* Fig. S3) (19). Finally, pose refinement was conducted in M (20), yielding an HA map at a global resolution of 8.9 Å from a set of 12,063 particles (Fig. 3*A* and *SI Appendix*, Fig S7). At this resolution, both isosurface and projection slices clearly show separation between individual HA protomers and individual helices within HA2 (Fig. 3 *A* and *C*). Furthermore, we could observe density corresponding to the viral membrane at lower contours (Fig. 3*A*). Our reconstruction resembles reported HA structures (4, 5, 8, 21, 22), showing a trimeric protein with three-fold symmetry and of approximately 14 nm in height and 8 nm in width. However, flexible fitting of a PR8 HA ectodomain crystal structure into the map showed subtle relaxation of the head domain and constriction of the stem, with a global RMSD of 1.89 Å (Movie S3). Likely, the constriction of the stem domain corresponds to tethering from the transmembrane helices and cytoplasmic tail that is not present in the crystal structure. Taken together, these data represent the highest-resolution view of virion-anchored HA obtained by cryoET to date.

Neighboring HA Trimers form a HA1–HA1 Interface Orchestrated by Mirrored Electrostatic Interactions. We subsequently investigated the configuration of trimers seen in LSTc-bound samples using subtomogram averaging of influenza virions incubated with 100 μM LSTc and 6.5 mM LSTc (Fig. 4). Refined coordinates from the bin4 reconstruction (Fig. 2 *C* and *D*) were used to extract bin2 particles. For both LSTc-bound samples, the triplet of HA trimers we described above persisted at higher-resolution reconstructions (Fig. 4*A*). We performed three independent refinements for the sample with 6.5 mM LSTc using central HA alone, central HA and the closest HA partner (pair I), and central HA plus the second closest HA partner (pair II). At this resolution, LSTc density cannot be unambiguously assigned.

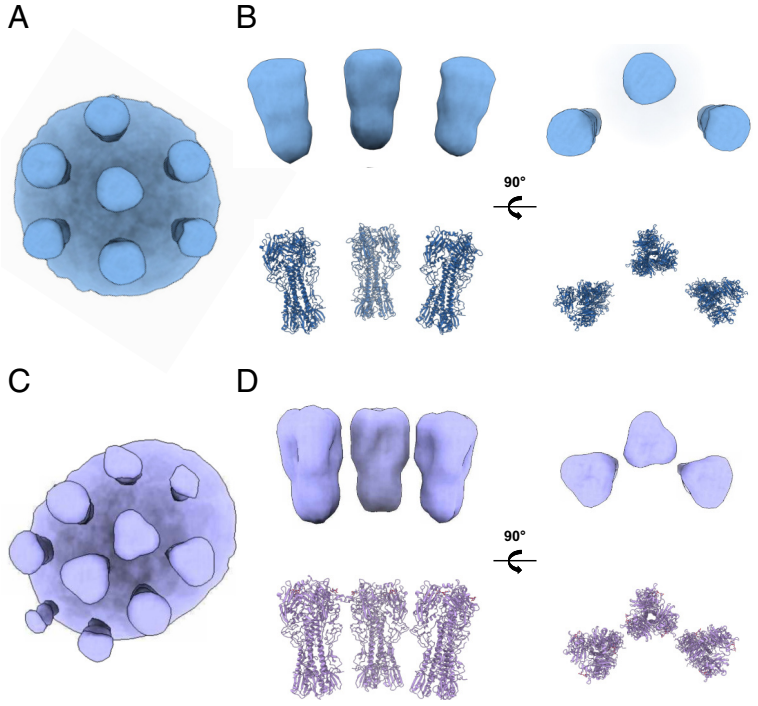

Fig. 2. Subtomogram averaging of HA reveals altered glycoprotein organization upon receptor recognition. (*A*) Top view of a bin4 reconstruction depicting a HA patch from PR8; reconstruction is looking down at a patch of HA glycoproteins atop the viral membrane. Untreated influenza has regular organization of HAs whereas LSTc-bound influenza has clustered HAs. (*B*) Zoom in view of three central HAs from PR8 virions. (*Upper*) The side and top views are presented. (*Lower*) Crystal structures of PR8 HA (PDB: 1RU7) fitted into the reconstruction. (*C*) Top view of a bin4 reconstruction depicting a HA patch from PR8 virions incubated with LSTc; reconstruction is looking down at a patch of HA glycoproteins atop the viral membrane. (*D*) Zoom in view of three central HAs from PR8 virions incubated with LSTc. (*Upper*) The side and top views are presented. (*Lower*) Crystal structures of PR8 HA bound to LSTc (PDB: 1RVZ) fitted into the reconstruction. Terminal sialic acid is shown as sticks. PR8 reconstructions and models are shown in light blue and PR8 + LSTc reconstructions and models are shown in lavender.

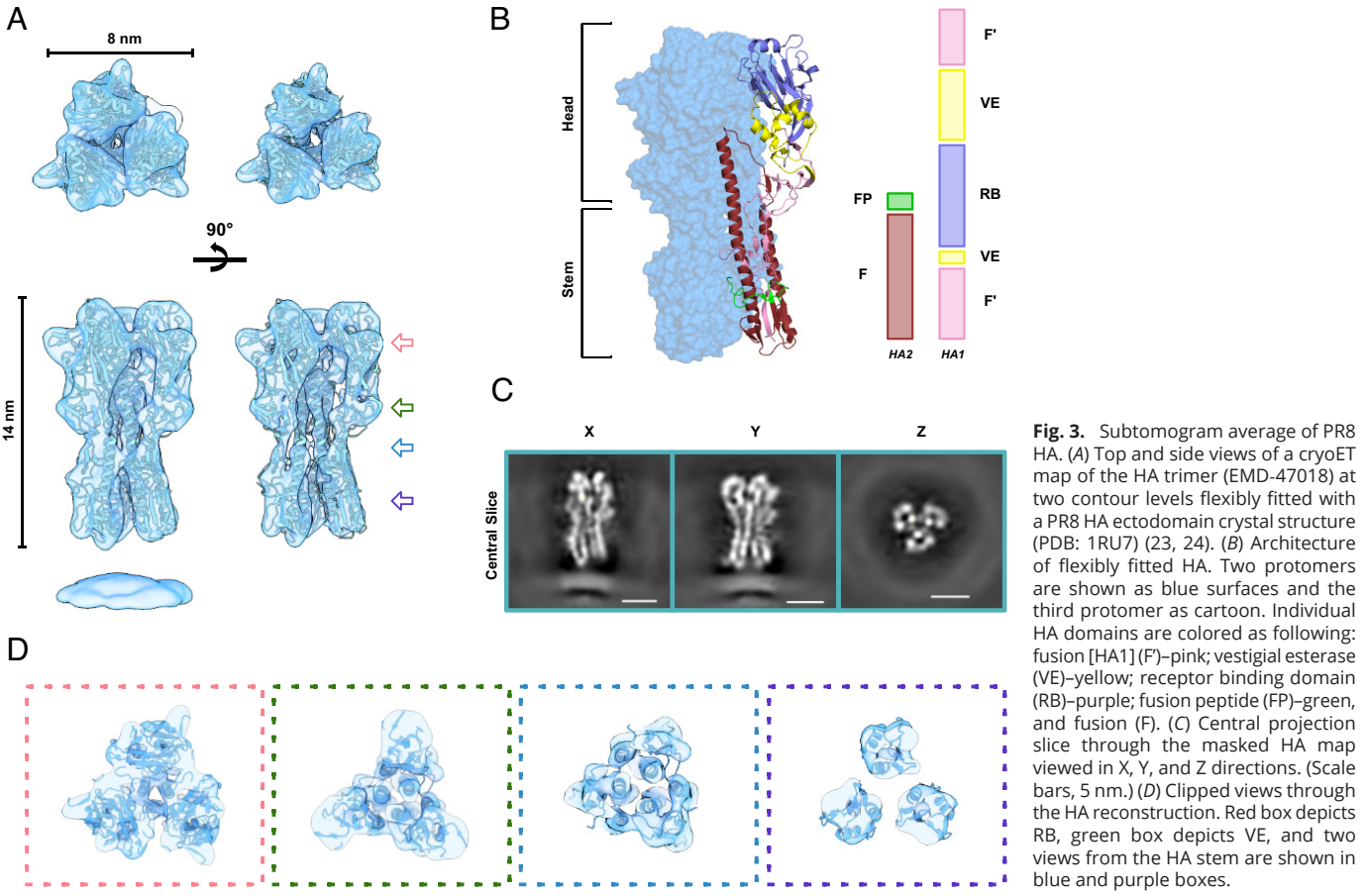

Fig. 3. Subtomogram average of PR8 HA. (*A*) Top and side views of a cryoET map of the HA trimer (EMD-47018) at two contour levels flexibly fitted with a PR8 HA ectodomain crystal structure (PDB: 1RU7) (23, 24). (*B*) Architecture of flexibly fitted HA. Two protomers are shown as blue surfaces and the third protomer as cartoon. Individual HA domains are colored as following: fusion [HA1] (F')–pink; vestigial esterase (VE)–yellow; receptor binding domain (RB)–purple; fusion peptide (FP)–green, and fusion (F). (*C*) Central projection slice through the masked HA map viewed in X, Y, and Z directions. (Scale bars, 5 nm.) (*D*) Clipped views through the HA reconstruction. Red box depicts RB, green box depicts VE, and two views from the HA stem are shown in blue and purple boxes.

Subtomogram averaging of the central HA reached a global resolution of 8.5 Å with 17,266 particles (*SI Appendix*, Fig. S7). Both HA1 and HA2 domains were well defined at this resolution, as well as secondary structure elements, especially in HA1 (Fig. 4*B*). Similar to the receptor-free HA reconstruction, we were able to trace α-helices at this subnanometer resolution. While we saw similar relaxation in the head domain and constriction within the stem domain as in the receptor-free HA, there were no additional domain rearrangements we could detect within receptor-bound HA.

To further refine our particle set, we conducted another round of 2D classification to remove approximately 25% of particles where the two neighboring HAs were further away from the central HA (*SI Appendix*, Fig. S6). The remaining 12,379 particles were centered on pair I and subjected to refinement, with the final map at C1 symmetry reaching 8.9 Å resolution (*SI Appendix*, Fig. S7). Inspecting the reconstruction for pair I, we confirmed the appearance of a HA1–HA1 interface between the two HA trimers (Fig. 4*C*). The two HA molecules were mirror image of one another, with the head domain of one protomer coming in proximity with the adjacent HA head. Between the two HAs, the flexible loop of the two receptor-binding regions and the loops were antiparallel to each other (Fig. 4*C*). Moreover, our reconstruction of pair I from virus incubated with 100 μM LSTc was nearly identical (Fig. 4*E*). For both maps, density was weaker in the stem region of the protomer facing the central HA, indicating possible flexibility in the region.

We observed a similar interface for pair II (Fig. 4*D*). The final reconstruction contained a set of 10,548 particles and reached a resolution of 10 Å (*SI Appendix*, Fig. S7). Density for the adjacent HA was weaker in comparison to the adjacent HA of pair I, and this weaker density was represented by its lower local resolution (*SI Appendix*, Fig. S7). Likely, there was more flexibility in the adjacent HA as the inter-HA distances also showed the adjacent HA in pair 1 was closer than that of pair 2 (*SI Appendix*, Fig. S5). However, it was apparent that the two neighbor-facing protomers of the central HA engaged its opposing domains similarly, with the globular heads packing against each other (Fig. 4 *C* and *E*). Taken together, we found the formation of an inter-HA interface arrangement that could enhance efficient receptor-binding and cell entry.

Molecular Details of Interactions That Mediate Clustering of Receptor-Bound HA. Finally, we investigated the interaction interfaces of receptor-bound HA (Fig. 5). To define HA–HA interfaces, we flexibly refined crystal structures of LSTc-bound HA within our reconstructions, and the refined models underwent energy minimization to determine optimal contacts. The two interfaces were both located within HA1, one in the receptor-binding domain and the second at the end of the vestigial esterase domain. Residing just outside of the receptor-binding site and implicated in neutralizing antibody interactions (25), the 140-loop constitutes the first interface (Fig. 5*B*). Glu142 is the main driver of this network, forming a salt bridge with Arg149' and hydrogen bonds with His141' and its mirroring residue, Glu142' (Fig. 5*C*). Within the lower interface, His276 forms hydrogen bonds with Glu277' of the opposing protomer, and vice versa (Fig. 5*D*). Altogether, our subtomogram averages provide strong evidence that these polar and electrostatic interactions drive interface contacts between adjacent HA trimers, and help promote the stable triplet of trimer HA configuration upon receptor binding (Fig. 6).

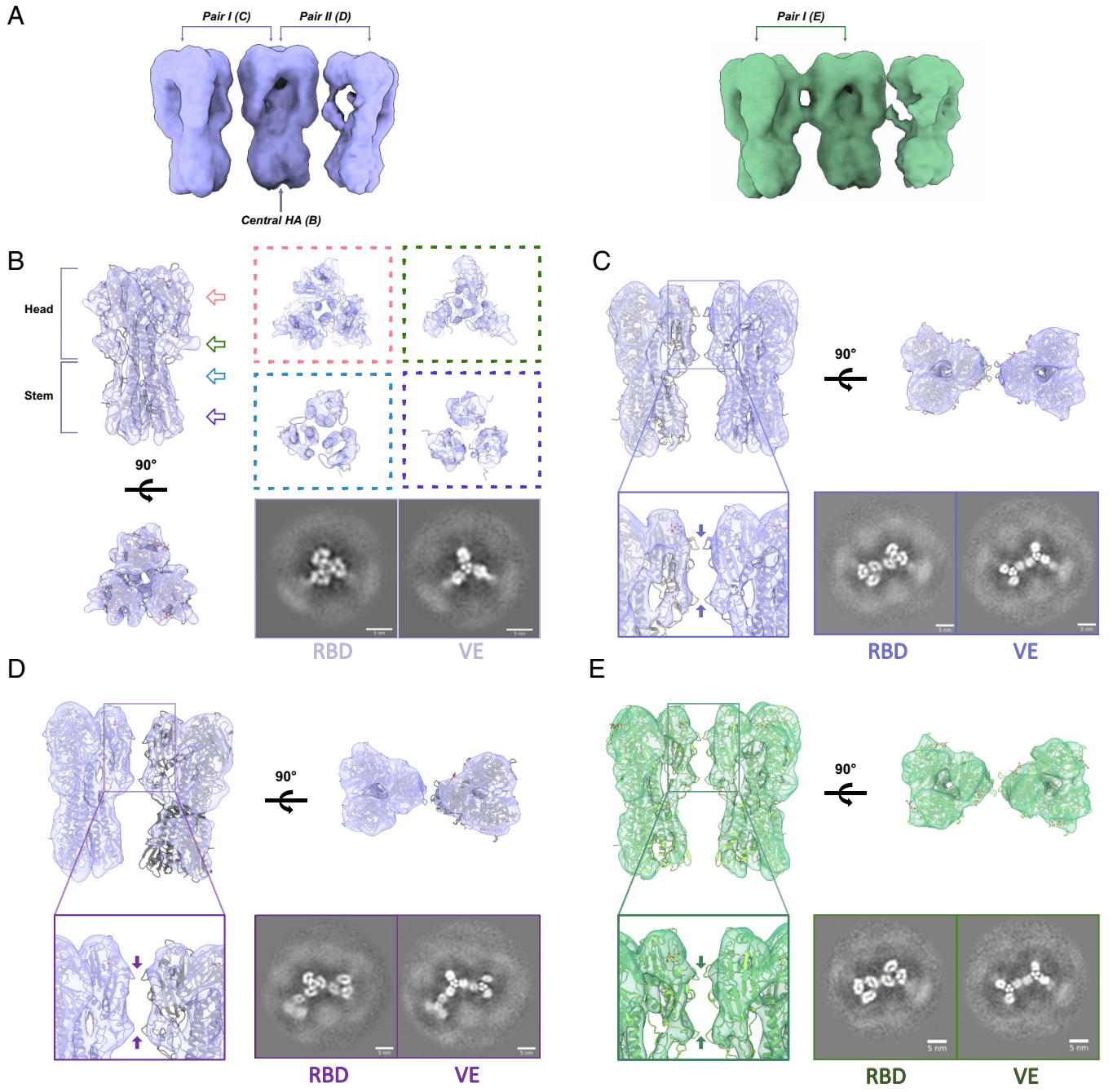

Fig. 4. Receptor binding induces inter-HA contacts but not intra-HA domain rearrangement. (*A*) Reconstruction of HA trimer of trimers incubated with (*Left*) 6.5 mM LSTc or (*Right*) 100 μM LSTc. Maps were obtained using bin2 particles. (*B*) (*Left*) Top and side views of the central HA in the trimer of HAs. (*Upper Right*) Clipped views through the HA reconstruction. Red box depicts RB, green box depicts VE, and two views from the HA stem are shown in blue and purple boxes. (*Lower Right*) Central projection slice through the HA map at the RB and VE domains. (*C–E*) (*C*) Pair I in the trimer of HAs. (*D*) Pair II in the trimer of HAs. (*E*) Pair I in the trimer of HAs from virions incubated with 100 μM LSTc. (*Upper*) Side and top views of each map were flexibly fitted with two copies of a PR8 HA ectodomain crystal structure bound to LSTc (PDB: 1RVZ) (23, 24). (*Inset*) zoomed in view of RB and VE interfaces highlighted by arrows. (*Lower Right*) Central projection slice through each reconstruction at the RB and VE domains. All scale bars are 5 nm.

Discussion

In summary, our study uses cryoET to illustrate receptor binding to native virions, which is an initial step of influenza virus infection. Through tomographic analysis and subtomogram averaging, we observed rearrangement of the HA glycoprotein array, resulting in HA clustering to form a triplet of trimers. We also characterized a previously undetected HA–HA interface that emerges upon receptor binding. These analyses gave rise to several subnanometer resolution subtomogram averages of influenza HA, including 1) the highest reported resolution of a virion-anchored HA subtomographic reconstruction and 2) the elucidation of the structure of virion-anchored HA in the presence of a cellular receptor mimic.

Consistent with previous studies, influenza virions exposed to a sialic acid containing receptor mimic did not exhibit any morphological changes in the virion (26–28). While there is overall density encompassing the receptor binding pocket, we were unable to observe distinct sialic acid density in our 8.5 to 10 Å reconstructions, as only secondary structures could be resolved at this

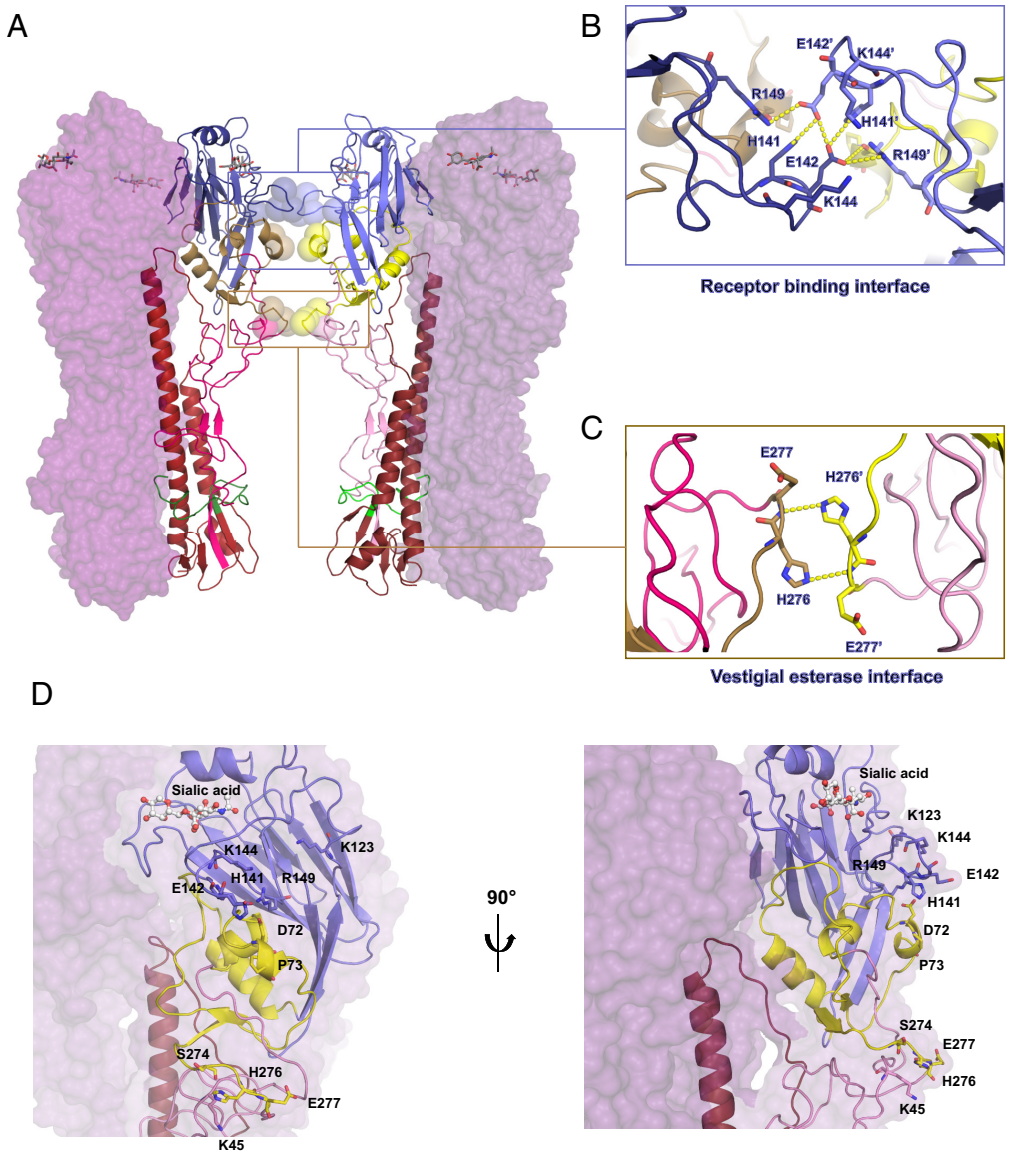

Fig. 5. HA–HA interface reveals mirror image contacts within HA1. (*A*) Model of interacting HA pair. Two protomers from each HA trimer are represented as a purple surface and the third as color-coded cartoon. Terminal sialic acids are represented as sticks. Domains are colored as according to the key in Fig. 3. Residues within 5 Å of the neighboring protomer are shown as spheres. (*B*) Zoomed-in view of receptor binding domain interactions. Hydrogen and ionic bonds are shown as yellow dashed lines. (*C*) Zoomed-in view of vestigial esterase domain interactions. Hydrogen and ionic bonds are shown as yellow dashed lines. (*D*) Zoomed-in view of proximal residues indicated as spheres in (*A*). Terminal sialic acids are shown as stick and balls.

resolution range. However, we observed changes in HA organization on the viral surface upon receptor binding, whereby receptor binding brought HA trimers closer together to form a triplet of trimers. We also found that upon receptor binding, an interface formed between HA protomers in neighboring HA trimers as they cluster.

This receptor-triggered clustering is likely functionally relevant. Previous studies have established that influenza virions bind cell surface sialic acid–containing cellular receptors multivalently (2, 29–31). This multivalent attachment increases the possibility that clustering of neighboring HAs would further enhance binding by allowing the virion to bind to an entire patch of surface glycans. Thus, we propose that once receptor-bound, dynamic HA movements become stabilized and form steady interactions with adjacent trimers to prepare for membrane fusion. We do not, however, observe large domain-level rearrangements within singular HA trimers, which is consistent with previous crystallographic studies and with biophysical studies that observe stochastic HA activation during fusion (5, 12). However, this process may be accompanied by smaller secondary structures and local changes, as these types of changes are beyond the resolution of the current study. Nevertheless, we visualized highly packed HA trimers cluster on the virion surface and impact the structure and organization of neighboring glycoproteins, as was previously proposed but not observed (32). It is likely that, given HA's millimolar affinity for sialic acid, HA clustering in the presence of its receptor enhances multivalent binding to productively achieve cellular entry. This phenomenon may explain why we see similar HA clustering in conditions where influenza virion was incubated with both saturating and subsaturating levels of LSTc. One hypothesis is that receptor binding may induce structural changes within HA1, both directly within the receptor-binding domain and allosteric motions that ripple through the rest of the glycoprotein. These changes may cause increased interactions with adjacent HAs that eventually lead to clustering. Moreover, previous molecular dynamics simulations of influenza have shown that the HA ectodomain undergoes various degrees of tilting on the viral surface (32). Within this context, the clustering we observe could act as stabilization for HA. Upon receptor binding,

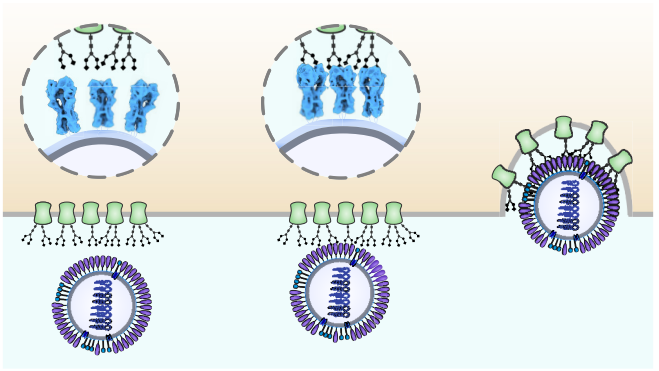

Fig. 6. Model of influenza HA binding and entry. Influenza virions travel within the respiratory tract prior to cellular entry. During this stage, HAs are capable of movement as the virions tumble to better sense the environment. Upon contact with the sialylated cell surface, local coordination of neighboring HAs allows for multivalent interaction with the cell within the contact region to induce productive cellular entry.

inter-HA clustering may arrest excessive tilting of HA and favorably position adjacent HAs to interact with additional sialic acid molecules. Thus, even local changes, such as receptor binding initially on one HA, could cause a rippling avidity effect through the viral surface to promote entry into the cell.

Interestingly, coordination between neighboring HAs is relevant in the context of other processes beyond receptor binding. Over the past two decades, investigations of HA coordination during the later membrane fusion steps have shown that approximately three HA molecules have been shown by kinetics to form a local fusion cluster that are required for fusion between endosomal and viral membranes (11–14). During acidification in an infected endosome, one HA can start the fusion process via insertion into the target membrane, but membrane fusion occurs rapidly only after two to three additional proximal HA molecules enter hemifusion. Thus, our full viral reconstructions corroborate and support the formation of a fusion cluster during influenza infection by a receptor-bound HA cluster consisting of three adjacent HA trimers on the virion surface tilting toward each other and thereby provide additional insights into the influenza entry pathway.

Our study further demonstrates the intricacies of the influenza entry pathway and shows additional dynamics of HA during receptor binding. We characterized the reorganization of glycoprotein packing on the virion surface upon sialic acid engagement and revealed a previously unseen formation of a triplet of HAs. Through subtomogram averaging of influenza HA, we reconstructed the highest-resolution virion-anchored HA reported, and receptor-bound HA reconstructions from whole virions. These maps allowed us to describe an interface between adjacent HAs that is established post receptor binding. In conclusion, this report provides the structural view of the intact, receptor-bound influenza virions, and provides further evidence that HAs orchestrate a coordinated mechanism for optimal viral entry. We anticipate that better understanding of HA cooperativity will advance our understanding of the molecular determinants of a successful infection and illuminate additional strategies for therapeutic development.

Materials and Methods

Virus and Reagents. A/PR/8/34 (PR8) influenza virus was grown in embryonated chicken eggs and purchased from Charles River Laboratories (Now AVS Bio. Catalog #: 10100374) and stored at −80 °C before use. LS-Tetrasaccharide c (LSTc) was purchased from Dextra (Catalogue #: SLN506) and stored at −20 °C before use.

Cryo-ET Sample Preparation and Tilt-Series Data Collection. PR8 influenza virus was diluted to 1 mg/mL or 0.5 mg/mL, and receptor-bound samples were incubated with 100 μM or 6.5 mM final LSTc concentration. Virus was mixed with BSA-coated 10 nm colloidal gold (Sigma-Aldrich) and 3 μL were applied to glow-discharged R2/2 holey carbon copper grids (Quantifoil). These grids were manually backblotted for 2 to 3 s with filter paper and rapidly frozen in a liquid ethane/propane mixture using an EMS-002 rapid immersion freezer. Prior to imaging, vitrified grids were stored in LN2. Grids were imaged on a Thermo Fisher Scientific Titan Krios electron microscope operating at 300 kV with a K3 camera (Gatan, Pleasanton) and a Gatan energy filter at a slit width of 20 eV centered on the zero-loss position. Tilt series of PR8 alone and PR8 with 100 μM LSTc were recorded from 0 to ±66° in 2-degree increments at a magnification of 42,000× (corresponding to a calibrated 2.09 Å of pixel size) using a dose symmetric scheme (33). Raw movies of these samples were acquired at an electron dose of 1.86 $e^-/Å^2$. Tilt series of PR8 incubated with 6.5 mM LSTc were recorded from 0 to ±51° in 3-degree increments at the same magnification. Raw movies of this sample were acquired at an electron dose of 3 $e^-/Å^2$. The sample was imaged in counting mode at each tilt angle as movies (four to six frames), and the accumulated dose of all movies was 120 $e^-/Å^2$. The defocus range of all tilt series is 4 to 8 μm. Data were acquired automatically under a low-dose mode using the SerialEM software (34).

Tilt-Series Preprocessing and Tomogram Generation. Raw movies were imported into Warp (v1.1beta) (18), where movie frame alignment and CTF estimation were carried out. Dose-weighted tilt series were exported from Warp and imported into IMOD for batched fiducial-based tilt series alignment (35). Aligned stacks were reimported into Warp for tomogram reconstruction at bin4 (8.35 Å/pixel).

Tomographic Analysis. Tomograms were imported into EMAN2.99 and preprocessed to enhance features for subsequent convolutional neural network-based segmentation and particle picking (36). Posttraining, HA particle coordinates from each tomogram were saved and modeled as 3D point clouds using the Open3D library (37). Outlier points were removed from point clouds based on the SD of a point's distance from its closest neighbors from the average distances across the point clouds; this step ideally removes misannotated particles. The agglomerative clustering algorithm implemented in the Scikit-Learn library (38) were used to generate single virion point clouds which were then exported as STL surfaces for automated virion morphology calculations in UCSF Chimera using the Measure and Color Blobs Tool, which prints out the axes of each virion (39).

To filter out virions that did not contain the M1 protein, HA and M1 coordinates were imported as point clouds. Proximity to M1 was used as a metric to conduct distance-based filtering of HA points, and HA coordinates more than 10 nm away from its nearest M1 coordinate were discarded for subtomogram averaging. Finally, single virion point clouds were imported into a Dynamo v1.15 environment within MATLAB R2023a for initial Euler angle estimation (40). The surface normal for each HA coordinate was calculated and its equivalent rotation matrix was converted into Euler angles. To generate Warp compatible metadata, Euler angles were converted from Dynamo to Relion convention using the *eulerangle* library and were written into a star file with its corresponding coordinate using the *starfile* library (41).

Subtomogram Averaging. Initially, HA subtomograms were extracted at a pixel spacing of 8.35 Å and a box size of 48 pixels. This box is large enough to encompass a 3 × 3 array of membrane-embedded influenza glycoproteins. An initial subtomogram average was generated through reference-free subtomogram averaging of a subset of 1,000 subtomograms in Relion 4.0 (19). This average was used as reference for subtomogram alignment of the entire dataset. After several rounds of 3D autorefine in Relion 4.0, 2D classification was carried out on aligned subtomograms to further identify outliers and nonaligned particles. This 2D classification step uses project images obtained from subtomograms, which represent a much faster way to conduct classification in comparison to 3D classification. These particles and duplicate particles were subsequently discarded. This subtomogram averaging scheme was carried out for subtomograms extracted at 4.17 Å/pixel and 2.8 Å/pixel, with more restricted angular sampling. After subtomogram averaging converged at 2.8 Å/pixel, subtomogram coordinates were imported into M v1.1beta and three rounds of particle pose refinement were carried out (20). Finally, subtomograms were exported at 2.1 or 2.2 Å/pixel and aligned in Relion 4.0, and after import into M, particle pose refinement, image warp grid (8x8 resolution), and stage angles were refined for three iterations. For all M refinement steps, three subiterations were carried out and 40% of available resolution was used for the first subiteration.

The subtomogram averaging pipeline for LSTc-bound HA samples was largely similar to HA alone. However, different masks were used at each stage to include density for neighboring HA trimers instead of just the central HA trimer. Resolution of all final maps was estimated using the criterion of FSC = 0.143 for masked and unmasked maps (42, 43). Local resolution range of maps were estimated using M (20).

Inter-HA distances for both HA and LSTc-bound HA were calculated using a custom Python script. Briefly, local subtomogram alignment was performed for each central HA and its two closest neighbors, where the HA was placed at the center of the subtomogram. Postalignment, inter-HA distances were measured from the center of each box, at the approximate location of the HA trimeric interface.

To generate models, crystal structures of PR8 HA (PDB: 1RU7) and PR8 HA bound to LSTc (PDB: 1RVZ) was rigid body docked into our HA and HA–LSTc maps, respectively using UCSF ChimeraX (23). Postrigid body fitting, real space refinement was conducted using the Phenix software package (24). Five rounds of global minimization, local rotamer fitting, occupancy refinement, and group ADP refinement were conducted. Energy minimization of the dimer of HAs model was performed using the OPLS2005 force field to a RMSD of 0.3 Å using the Schrodinger Protein Preparation Wizard (44, 45).

Visualization. 3dmod was used to generate snapshots and movies of tomograms (35). UCSF ChimeraX (23) was used to visualize tomograms and subtomogram averages. PyMOL was used to visualize HA–HA interfaces (46). Seaborn and Matplotlib libraries were used to generate histograms (47, 48).

Code. Custom Python scripts used for metadata conversion, starfile generation, interglycoprotein spacing calculation, and virion surface model generation are publicly available on Github (https://github.com/jqyhuang/influenza-analysis).

Data, Materials, and Software Availability. Subtomogram averages and representative tomograms are deposited at the EMDB under the accession numbers EMD-47018 (49), EMD-47027 (50), EMD-47028 (51), EMD-47029 (52), EMD-47030 (53), EMD-49095 (54), and EMD-49096 (55). A model of the dimer of HA trimers model is deposited at the PDB under the accession number 9N8P (56). Raw tiltseries are deposited at EMPIAR under the accession number EMPIAR-12543 (57) and EMPIAR-12544 (58). Original code used for analysis has been deposited at Zenodo (DOI: 10.5281/zenodo.14841177) (59). Any additional information required to reanalyze the data reported in this paper is available from the corresponding authors upon request. All original maps will be shared with reviewers.

ACKNOWLEDGMENTS. We would like to acknowledge helpful discussions with the members of the Kelch, Munro, Grigorieff, and Schiffer labs, especially Matthew Unger, Clint McDaniel, and Drs Sabihur Rahman Farooqui and Nese Kurt Yilmaz. We would also like to thank the UMass Chan cryoEM Core facility for their help with data acquisition and for providing us with support and advice. We would like to acknowledge Life Science Editors, especially Dr. Milka Kostic, for editing the manuscript. National Institute of General Medical Sciences R01GM143773 (J.B.M. and M.S.), National Institute of General Medical Sciences R35GM151996 (C.A.S.)

1. F. Krammer *et al.*, Influenza. *Nat. Rev. Dis. Primers* **4**, 3 (2018).
2. M. Mammen, S. K. Choi, G. M. Whitesides, Polyvalent interactions in biological systems: Implications for design and use of multivalent ligands and inhibitors. *Angew. Chem. Int. Ed. Engl.* **37**, 2754–2794 (1998).
3. N. C. Wu, I. A. Wilson, Influenza hemagglutinin structures and antibody recognition. *Cold Spring Harb. Perspect. Med.* **10**, a038778 (2020).
4. Y. Ha, D. J. Stevens, J. J. Skehel, D. C. Wiley, X-ray structures of H5 avian and H9 swine influenza virus hemagglutinins bound to avian and human receptor analogs. *Proc. Natl. Acad. Sci. U.S.A.* **98**, 11181–11186 (2001).
5. S. J. Gamblin *et al.*, The structure and receptor binding properties of the 1918 influenza hemagglutinin. *Science* **303**, 1838–1842 (2004).
6. R. J. Russell, D. J. Stevens, L. F. Haire, S. J. Gamblin, J. J. Skehel, Avian and human receptor binding by hemagglutinins of influenza A viruses. *Glycoconjugate J.* **23**, 85–92 (2006).
7. D. K. Das *et al.*, Direct visualization of the conformational dynamics of single influenza hemagglutinin trimers. *Cell* **174**, 926–937.e12 (2018).
8. Q. J. Huang *et al.*, Quantitative structural analysis of influenza virus by cryo-electron tomography and convolutional neural networks. *Structure* **30**, 777–786.e3 (2022).
9. S. Wasilewski, L. J. Calder, T. Grant, P. B. Rosenthal, Distribution of surface glycoproteins on influenza A virus determined by electron cryotomography. *Vaccine* **30**, 7368–7373 (2012).
10. E. E. H. Tran *et al.*, Cryo-electron microscopy structures of chimeric hemagglutinin displayed on a universal influenza vaccine candidate. *mBio* **7**, e00257 (2016).
11. D. L. Floyd, J. R. Ragains, J. J. Skehel, S. C. Harrison, A. M. van Oijen, Single-particle kinetics of influenza virus membrane fusion. *Proc. Natl. Acad. Sci. U.S.A.* **105**, 15382–15387 (2008).
12. T. Ivanovic, J. L. Choi, S. P. Whelan, A. M. van Oijen, S. C. Harrison, Influenza-virus membrane fusion by cooperative fold-back of stochastically induced hemagglutinin intermediates. *Elife* **2**, e00333 (2013).
13. T. Ivanovic, S. C. Harrison, Distinct functional determinants of influenza hemagglutinin-mediated membrane fusion. *Elife* **4**, e11009 (2015).
14. J. J. Otterstrom *et al.*, Relating influenza virus membrane fusion kinetics to stoichiometry of neutralizing antibodies at the single-particle level. *Proc. Natl. Acad. Sci. U.S.A.* **111**, E5143–E5148 (2014).
15. G. L. Hendricks *et al.*, Sialylneolacto-N-tetraose c (LSTc)-bearing liposomal decoys capture influenza A virus. *J. Biol. Chem.* **288**, 8061–8073 (2013).
16. A. Harris *et al.*, Influenza virus pleiomorphy characterized by cryoelectron tomography. *Proc. Natl. Acad. Sci. U.S.A.* **103**, 19123–19127 (2006).
17. Q. Chen, X. Huang, R. Wei, L. Zhang, C. Yin, Characterization of influenza virus PR8 strain cultured in embryonated eggs by cryo-electron tomography. *Biochem. Biophys. Res. Commun.* **516**, 57–62 (2019).
18. D. Tegunov, P. Cramer, Real-time cryo-electron microscopy data preprocessing with Warp. *Nat. Methods* **16**, 1146–1152 (2019).
19. J. Zivanov *et al.*, A Bayesian approach to single-particle electron cryo-tomography in RELION-4.0. *Elife* **11**, e83724 (2022).
20. D. Tegunov, L. Xue, C. Dienemann, P. Cramer, J. Mahamid, Multi-particle cryo-EM refinement with M visualizes ribosome-antibiotic complex at 3.5 Å in cells. *Nat. Methods* **18**, 186–193 (2021).
21. N. K. Sauter *et al.*, Hemagglutinins from two influenza virus variants bind to sialic acid derivatives with millimolar dissociation constants: A 500-MHz proton nuclear magnetic resonance study. *Biochemistry* **28**, 8388–8396 (1989).
22. J. Stevens *et al.*, Structure and receptor specificity of the hemagglutinin from an H5N1 influenza virus. *Science* **312**, 404–410 (2006).
23. E. F. Pettersen *et al.*, UCSF ChimeraX: Structure visualization for researchers, educators, and developers. *Protein Sci.* **30**, 70–82 (2021).
24. P. D. Adams *et al.*, PHENIX: A comprehensive Python-based system for macromolecular structure solution. *Acta Crystallogr. D Biol. Crystallogr.* **66**, 213–221 (2010).
25. M. Hong *et al.*, Antibody recognition of the pandemic H1N1 Influenza virus hemagglutinin receptor binding site. *J. Virol.* **87**, 12471–12480 (2013).
26. J. Fontana, G. Cardone, J. B. Heymann, D. C. Winkler, A. C. Steven, Structural changes in Influenza virus at low pH characterized by cryo-electron tomography. *J. Virol.* **86**, 2919–2929 (2012).
27. J. Fontana, A. C. Steven, Influenza virus-mediated membrane fusion: Structural insights from electron microscopy. *Arch Biochem. Biophys.* **581**, 86–97 (2015).
28. J. Fontana, A. C. Steven, At low pH, influenza virus matrix protein M1 undergoes a conformational change prior to dissociating from the membrane. *J. Virol.* **87**, 5621–5628 (2013).
29. X. Xiong *et al.*, Receptor binding by a ferret-transmissible H5 avian influenza virus. *Nature* **497**, 392–396 (2013).
30. D. J. Benton, S. R. Martin, S. A. Wharton, J. W. McCauley, Biophysical measurement of the balance of influenza a hemagglutinin and neuraminidase activities. *J. Biol. Chem.* **290**, 6516–6521 (2015).
31. N. J. Overeem, P. H. Hamming, M. Tieke, E. van der Vries, J. Huskens, Multivalent affinity profiling: Direct visualization of the superselective binding of influenza viruses. *ACS Nano* **15**, 8525–8536 (2021).
32. L. Casalino *et al.*, Breathing and tilting: Mesoscale simulations illuminate influenza glycoprotein vulnerabilities. *ACS Central Sci.* **8**, 1646–1663 (2022).
33. W. J. H. Hagen, W. Wan, J. A. G. Briggs, Implementation of a cryo-electron tomography tilt-scheme optimized for high resolution subtomogram averaging. *J. Struct. Biol.* **197**, 191–198 (2017).
34. D. N. Mastronarde, Automated electron microscope tomography using robust prediction of specimen movements. *J. Struct. Biol.* **152**, 36–51 (2005).
35. D. N. Mastronarde, S. R. Held, Automated tilt series alignment and tomographic reconstruction in IMOD. *J. Struct. Biol.* **197**, 102–113 (2017).
36. M. Chen *et al.*, Convolutional neural networks for automated annotation of cellular cryo-electron tomograms. *Nat. Methods* **14**, 983–985 (2017).
37. Q.-Y. Zhou, J. Park, V. Koltun, Open3D: A modern library for 3D data processing. arXiv [Preprint] (2018). https://arxiv.org/abs/1801.09847 (Accessed 1 May 2024).
38. F. Pedregosa *et al.*, Scikit-learn: Machine Learning in Python. *J. Mach. Learn. Res.* **12**, 2825–2830 (2011).
39. E. F. Pettersen *et al.*, UCSF Chimera–A visualization system for exploratory research and analysis. *J. Comput. Chem.* **25**, 1605–1612 (2004).
40. D. Castaño-Díez, M. Kudryashev, M. Arheit, H. Stahlberg, Dynamo: A flexible, user-friendly development tool for subtomogram averaging of cryo-EM data in high-performance computing environments. *J. Struct. Biol.* **178**, 139–151 (2012).
41. A. Burt, L. Gaifas, T. Dendooven, I. Gutsche, A flexible framework for multi-particle refinement in cryo-electron tomography. *PLoS Biol.* **19**, e3001319 (2021).
42. G. Harauz, M. van Heel, Exact filters for general geometry three dimensional reconstruction. *Optik.* **73**, 146–156 (1986).
43. P. B. Rosenthal, R. Henderson, Optimal determination of particle orientation, absolute hand, and contrast loss in single-particle electron cryomicroscopy. *J. Mol. Biol.* **333**, 721–745 (2003).
44. W. L. Jorgensen, D. S. Maxwell, J. Tirado-Rives, Development and testing of the OPLS all-atom force field on conformational energetics and properties of organic liquids. *J. Am. Chem. Soc.* **118**, 11225–11236 (1996).
45. G. Madhavi Sastry, M. Adzhigirey, T. Day, R. Annabhimoju, W. Sherman, Protein and ligand preparation: Parameters, protocols, and influence on virtual screening enrichments. *J. Comp. Aided Mol. Design* **27**, 221–234 (2013).
46. Schrodinger, LLC, The PyMOL Molecular Graphics System (Version 1.8, Schrodinger LLC, 2015).
47. M. Waskom, seaborn: Statistical data visualization. *J. Open Source Softw.* **6**, 3021 (2021).
48. J. D. Hunter, Matplotlib: A 2D graphics environment. *Comput. Sci. Eng.* **9**, 90–95 (2007).
49. Q. J. Huang, C. A. Schiffer, Subtomogram average of hemagglutinin from influenza A virions. Electron Microscopy Data Bank. https://www.ebi.ac.uk/emdb/EMD-47018. Deposited 16 September 2024.
50. Q. J. Huang, C. A. Schiffer, Subtomogram average of hemagglutinin from influenza A virions incubated with 6.5 mM LSTc. Electron Microscopy Data Bank. https://www.ebi.ac.uk/emdb/EMD-47027. Deposited 17 September 2024.

51. Q. J. Huang, C. A. Schiffer, Subtomogram average of hemagglutinin with closest HA neighbour from influenza A virions incubated with 6.5 mM LSTc. Electron Microscopy Data Bank. https://www.ebi.ac.uk/emdb/EMD-47028. Deposited 17 September 2024.
52. Q. J. Huang, C. A. Schiffer, Subtomogram average of hemagglutinin with second closest HA neighbour from influenza A virions incubated with 6.5 mM LSTc. Electron Microscopy Data Bank. https://www.ebi.ac.uk/emdb/EMD-47029. Deposited 17 September 2024.
53. Q. J. Huang, C. A. Schiffer, Subtomogram average of hemagglutinin with closest HA neighbour from influenza A virions incubated with 100 uM LSTc. Electron Microscopy Data Bank. https://www.ebi.ac.uk/emdb/EMD-47030. Deposited 17 September 2024.
54. Q. J. Huang, K. Song, C. A. Schiffer, M. Somasundaran, Representative tomogram of LSTc-bound influenza virions. Electron Microscopy Data Bank. https://www.ebi.ac.uk/emdb/EMD-49095. Deposited 6 February 2025.
55. Q. J. Huang, K. Song, C. A. Schiffer, M. Somasundaran, Representative tomogram of influenza (PR8/34). Electron Microscopy Data Bank. https://www.ebi.ac.uk/emdb/EMD-49096. Deposited 6 February 2025.
56. Q. J. Huang, K. Song, C. A. Schiffer, M. Somasundaran, Subtomogram average of dimers of influenza HA trimers. Protein Data Bank. https://www.rcsb.org/structure/9N8P. Deposited 9 February 2025.
57. Q. J. Huang, K. Song, C. A. Schiffer, M. Somasundaran, Cryo electron tomography of PR/8/34 influenza A virus. The Electron Microscopy Public Image Archive. https://www.ebi.ac.uk/empiar/EMPIAR-12543/. Deposited 6 February 2025.
58. Q. J. Huang, K. Song, C. A. Schiffer, M. Somasundaran, Cryo electron tomography of PR/8/34 influenza A virus incubated with LSTc glycan. The Electron Microscopy Public Image Archive. https://www.ebi.ac.uk/empiar/EMPIAR-12544/. Deposited 6 February 2025.
59. Q. J. Huang, jqyhuang/influenza-analysis. Zenodo. https://zenodo.org/records/14841177. Deposited 5 May 2022.